ELSEVIER

Ultramicroscopy 86 (2001) 31–38

ultramicroscopy

www.elsevier.nl/locate/ultramic

A model for the hillock formation on graphite surfaces by 246 MeV Kr^+ ions

P. Nagy[a,b,*], B. Szabó[c], Zs. Szabó[c], K. Havancsák[d], L.P. Biró[b], J. Gyulai[b]

[a] *Chemical Research Centre of Hungarian Academy of Sciences, P.O. Box 17, H-1525 Budapest, Hungary*
[b] *KFKI, Research Institute for Technical Physics and Materials Science, P.O. Box 49, H-1525 Budapest, Hungary*
[c] *Eötvös University, Pázmány P. sétány 2. H-1117 Budapest, Hungary*
[d] *Institute for Solid State Physics, Eötvös University, Pázmány P. sétány 1/A. H-1117 Budapest, Hungary*

Received 31 May 2000

Abstract

Scanning tunnelling microscopy has been used to study the effect of ion bombardment at different angles of incidence on a graphite surface. The 246 MeV energy of Kr^+ ions was selected in the medium energy range, where the electronic and nuclear stopping is nearly balanced. The low dose ($1 \times 10^{12}/cm^2$) of ions allows the characterization of single features caused by bombardment in perpendicular, at 30° and at 60° incidence. The density of hillocks caused by the ion bombardment is significantly lower than the ion dose and this density depends on the angle of incidence. The hillocks are attributed to knocked-on atoms leaving the sample surface. A simple model for the scattering process is presented to enlighten the hillock density differences. Other features produced by the ion bombardment, such as elongated traces and $(\sqrt{3} \times \sqrt{3})$ R30 superstructures are also reported.

Keywords: Scanning tunnelling microscopy; Ion implantation; Hillock; Graphite

1. Introduction

The interaction of ion beams with surfaces has proven to be an important scientific problem in a range of fields, such as analytical techniques (secondary ion mass spectrometry, Rutherford Backscattering) and in technical applications (ion etching, thin film growth, implantation used in semiconductor industry and hardening structural materials). Considerable effort has been made to understand the process of slowing down of ions of different energy in a range of materials [1,2]. Structural changes, i.e. the damages produced in the target material are the most important consequence of this process: in some cases it is very useful, as for example in hardening structure materials [3], but the same process is undesired in ion thinning of TEM samples [4]. The damage production may be technologically useful for example in wave-guide production by damage-induced modification of optical properties, or highly undesirable as in microelectronics. Consequently, understanding the details of the interaction processes has essential importance.

Due to experimental and theoretical complexities, surface damage is one of the less

*Correspondence address: Chemical Research Centre of Hungarian Academy of Sciences, P.O. Box 17, H-1525 Budapest, Hungary. Tel.: +36-1-3257548; fax: +36-1-3257509.
E-mail address: nagyp@chemres.hu (P. Nagy).

0304-3991/01/$ - see front matter
PII: S0304-3991(00)00078-4

well-explored areas of atomic collisions in solids and its detailed atomic-scale mechanisms are not yet fully understood. Surface topography and defect structure caused by ion bombardment has been studied by scanning electron microscope (SEM) [5,6], transmission electron microscope (TEM) [7] and field ion microscope (FIM), but – due to the sample preparation or the instrument itself – these methods could not directly investigate the damaged surface in full detail.

Scanning probe microscopies (SPM) especially scanning tunnelling microscopy (STM) [8] and atomic force microscopy (AFM) [9] have been proved to be a powerful tool for studying surface damage with atomic or nearly atomic resolution in both lateral and vertical directions. Several papers have been published recently on the investigation of surface damage caused by ion bombardment [10–17]. In these studies various ions with energies ranging from several keV to several GeV were used; highly oriented pyrolytic graphite (HOPG), mica, PbS and Si were selected as target materials. In some of these studies the incident ions caused hillocks on the sample surface [10–12,18] while in the others craters were created [19]. Some authors reported $(\sqrt{3}\times\sqrt{3})$ R30 superstructures surrounding the ion impacts on the surface of HOPG [12,13,20].

The mechanisms responsible for damage production during the slowing down of an energetic ion are: electronic and nuclear stopping. Electronic stopping dominates the slowing down of high-energy ions (in the MeV range and above), being the interaction of the uncompensated electrical charge of the ion with the electrons of the target. The electronic stopping may cause the so-called thermal spikes [21] or in insulators, may lead to Coulomb explosion [22]. Nuclear stopping is dominant in the case of low-energy ions, in the keV range. In the case of 246 MeV Kr ions the electronic and nuclear stopping powers are 1.2×10^{4} and 1.6×10^{1} keV/μm, respectively. Investigation of these processes in this medium energy range is and will be very important for a better understanding of the ion–solid interactions.

The damage caused by ion bombardment was investigated previously mainly in perpendicular [18,23–25] or in parallel [16,26] incidence geometry related to the surface plane. The perpendicular incidence geometry characterizes the surface damage caused by the ions falling on the sample surface. In the second case the sample surface is parallel to ion beam, revealing the damage caused along the trajectory of the ions [26].

Despite the numerous experiments reported, still there is a lack of agreement concerning the surface damage production by ion bombardment, in particular the exact production mechanism of hillocks is still discussed [10,17]. Our goal was to contribute to a better understanding of the processes taking place in irradiated materials in the not so well-investigated 100 MeV energy and medium ion-mass range.

2. Experimental

We used HOPG as an ideal sample material for studying the effect of ion irradiation by tunnelling microscopy: its surface is easy to clean, inert and well suited for STM investigations. Considering that krypton ions have medium mass, large energy loss and are chemically inert, we used 246 MeV Kr^{+} ions to bombard the HOPG samples. Irradiations were performed at the U-400 cyclotron of JINR, in Dubna. Special care was taken to avoid sample contamination during sample preparation and after irradiation. Irradiations were carried out at room temperature, in a vacuum, with samples fixed onto a cooled metal surface. The ion flux was maintained at a relatively low level ($\approx 10^{9}$ ions/cm^2/s); thus, temperature increase during the irradiation did not exceed 15°C. The ion fluence attained was 10^{12} ions/cm^2, in order to minimize cascade overlap in the surface region but produce numerous defects on the irradiated surface. Three pieces of freshly cleaved 8×8 mm^2 HOPG samples were irradiated in the same run: one in perpendicular geometry (S1), one was tilted by 30° (S2) and one by 60° (S3) (Fig. 1). The samples were investigated by STM in an ambient atmosphere.

We found a high density of small hillocks on all three samples (Fig. 2) in agreement with Li et al. [17]. The shape of the hillocks does not show a clear dependence on the irradiation direction of

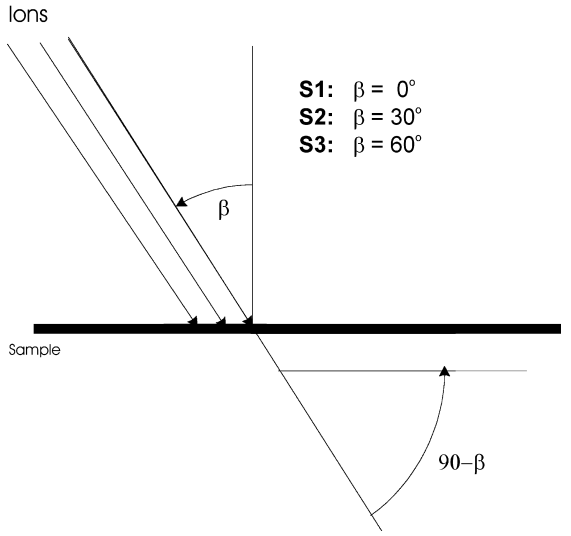

Fig. 1. Irradiation geometry of the three samples S1–S3. β is the incidence angle with respect to the normal.

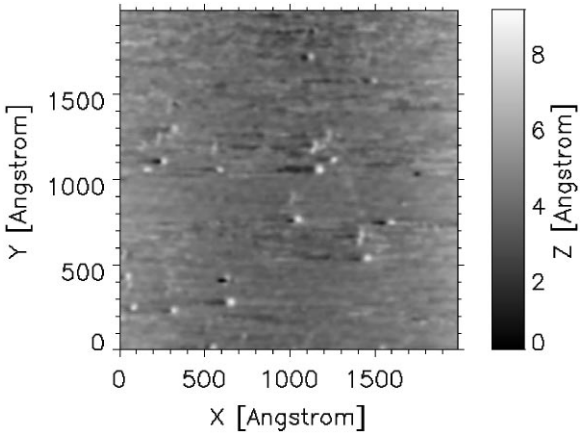

Fig. 2. Surface morphology of the ion-bombarded surface, top view, constant-current STM image of S1 sample (imaging parameters are $I_{\text{tunnel}} = 1$ nA, $U_{\text{Bias}} = 130$ mV, for all the STM images).

the sample. The height of hillocks is around 2 Å and the diameter is about 50 Å. Due to tip convolution effects the measured diameter of hillocks is strongly dependent on the actual tip shape of the STM so its spread is not characteristic for the real dimensions.

In contrast to shape and dimensions, the density of hillocks showed significant change between the samples. We counted the number of hillocks in about 10 images/sample (about 400 protrusions), calculated the average hillock density on the surface, and the number of hillocks generated per incident ion. The results are shown in Table 1.

Some hillocks were investigated in detail. Most of them were small bumps, as shown in Fig. 3. Protrusions surrounded by a wavy superstructure, as in Fig. 4, were also found. The origin of these structures is discussed in the next section. The features like that in Fig. 5 are attributed to the ion irradiation too, their height is the same as that of the hillocks, but they are about 100 Å long, and their surface density is much lower than the density of hillocks shown in Fig. 3. Similar features, sometimes several microns in length, have been found by AFM too [27,28]. These features are attributed to the channelling of some knocked-on C atoms.

3. Discussion

The use of HOPG as sample material enables us to directly compare our work to previous studies of atomic ion impact on graphite. These studies identified the formation of characteristic protrusions, hillocks of the graphite substrate arising from ion implantation [13–15,20,23,26–31]. There has been a discussion on the formation of craters and protrusions and on features emerging on the impact site of ions and on the sites where the secondary or higher-order knocked-on atoms leave the sample. There is no concord in the question, whether incident ions leave any track on the sample surface.

Table 1
Hillock statistics – measured hillock density on samples S1–S3 and the ratio of hillock density to ion dose. The row "Scatter" indicates the data scattering of counted number of hillocks per cm^2

Angle of incidence (deg)	0	30	60
Hillock density ($1/cm^2$)	6.6×10^{10}	1.12×10^{11}	1.17×10^{11}
Scatter ($1/cm^2$)	2×10^{10}	2×10^{10}	1×10^{10}
Number of hillocks per 1000 incident ions	66	112	117

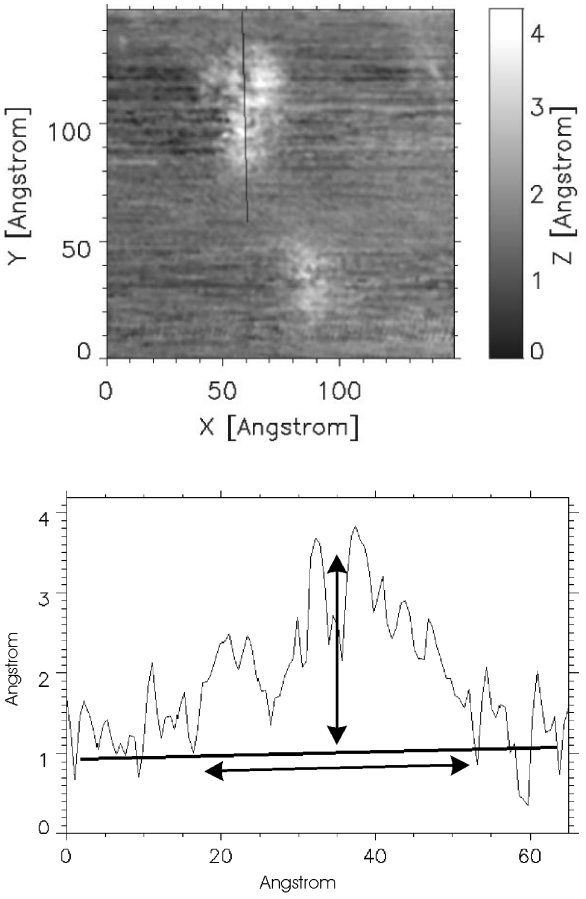

Fig. 3. Top view, constant-current STM image of hillocks. (a) Topographic image, the line marks the position of the line cut shown in (b). (b) The thick line in the figure shows the average surface height in the region of the feature. The dimensions marked by the arrows are 30 Å in the horizontal direction and 2 Å in the vertical direction.

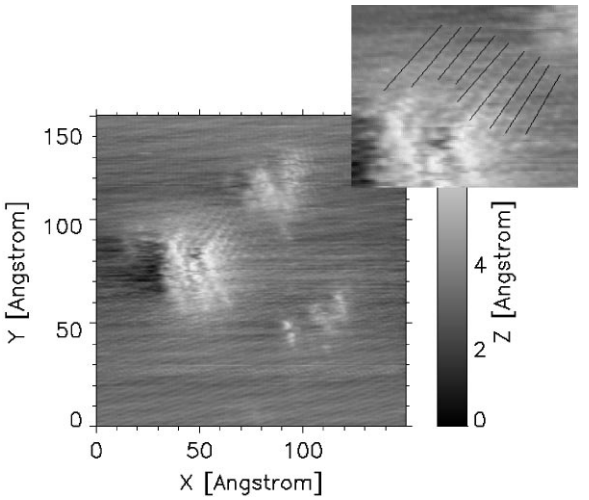

Fig. 4. Top view, constant-current STM image of superstructure around a hillock. The spacing of the lines measured in the figure is 4–4.6 Å.

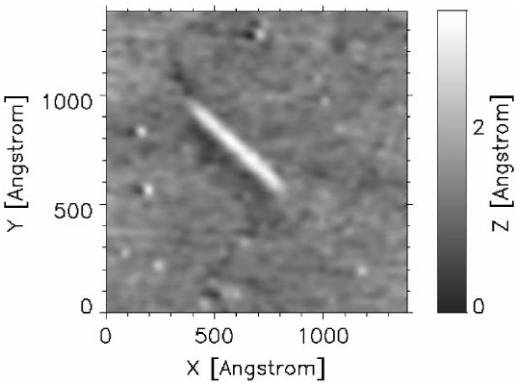

Fig. 5. Top view, constant-current STM image of the trace of channelling knocked-on C particle. Three hillocks are also visible in the image.

Several authors reported [10,17] that when using ion energies in the 500 eV–40 keV range the number of hillocks found in a certain area is almost equal to the number of ions falling on that area. Although there is disagreement regarding the mechanism by which the hillocks are produced [17], it is widely accepted that every incident ion itself generates a hillock. However, the experimental observation of 1 hillock/incident ion does not necessarily imply that the penetrating ion itself produced the hillock. One should not forget that a certain number of hillocks were produced by knocked-on target atoms which left the target crossing the irradiated surface. Moreover, as Li et al. [17] convincingly demonstrate, the energy density deposited in the surface region of the target is high enough for the production of non-linear cascades. Ogiso et al. [23] recently reported experimental evidence for the role of knocked-on target atoms in surface damage production during irradiation with several types of 3.1 MeV ions ranging from Si to Au. Their calculations show that in the keV energy range the probability of knocked-on atom generation in the first two layers

of the graphite target is near 1, i.e. the value of the hillock/incident ion ratio close to 1 could also be attributed to the damage produced by knocked-on atoms. On the other hand, the probability of knocked-on target atom generation in the MeV range is 10^{-2}–10^{-1}, in good agreement with the density of surface damage found by friction force microscopy [23].

In this work we found, that the majority of features seen on the surface have the typical shape for hillocks, and that the density of features counted on the surface is significantly lower than the ion dose. The ratio of hillocks to the number of incident ions is in the range 66×10^{-3}–117×10^{-3}, in agreement with calculations of Ogiso et al. (knocked-on atom generation probability – 10^{-2}–10^{-1}) [23]. According to these authors, for ions in keV range the nuclear stopping is dominant, and the ion loses its energy in a few atomic layers distance, giving a comparatively high probability of knocking out an atom or a small cluster in the vicinity of the surface. In the case of GeV ions the energy deposited by electronic stopping is very high, leading to a thermal spike, leaving a crater on the surface. In the energy range of 100 MeV there is no thermal spike in graphite and the cross-section for knock-on is low, so incident ions do not cause any defect in the surface.

We attribute the observed hillocks to the escape of primary or higher-order knocked-on atoms. To enlighten the physical and geometric relations we calculated the cumulative cross-section for scattering secondary particles back towards the sample surface for different incidence angles of primary ions. The calculations are discussed in detail in the appendix; here we give only a brief summary of the results. The maximum scattering angle of a knocked-on C particle with respect to the direction of the primary ion is 90°, so in the case of perpendicular incidence no C particle can escape the sample in a single scattering process. The hillocks found on sample S1 are attributed to multiple scattering processes, a case not accounted for in our calculations. The model used to calculate the surface density of features for oblique incidences produced by knocked-on C atoms is based on the following assumptions: (i) in order to reach the sample surface the value of scattering angle for the primary knocked-on C atoms has to be in the range [90°, (90°$-\beta$)] (Fig. 1); (ii) a knocked-on C atom needs the energy $E_C^{\min}$ to leave the sample. The number of knocked-on atoms crossing the surface of the sample was calculated by integrating the differential cross-section given by [2,32] according to the above conditions (see the appendix for more details). According to our simple model, at normal incidence no features should be produced due to primary knocked-on atoms. Therefore, the observed features are attributed to multiple scattering events. We calculated the above-mentioned cross-section based on the Rutherford formula (unscreened Coulomb potential) and also on the Thomas-Fermi and Bohr screened potentials. The results for different potentials are different, but they have the common characteristic of falling rapidly toward the perpendicular incidence and having comparatively small difference between 30° and 60° incidence, as the measured data do (Fig. 6). (The results of calculations based on the scattering potentials are scaled to the measured data at 60° incidence.)

In Fig. 3 two hillocks are enlarged, and the cross-section of one of them is drawn. The height of all of the hillocks we investigated was in the range of 1–2 Å, and the diameter was in the 20–50 Å range. In Fig. 4a superstructure is imaged around a hillock. Such features were found on each of our samples a few times during our work. The image in Fig. 4 is too noisy to resolve the atomic structure of the HOPG, but the superstructure is clearly visible with a periodicity of 4–4.6 Å. This periodicity is close to that of the superstructure caused by ad-atoms on HOPG surface, explained by Mizes as charge density oscillations [33] and investigated by several researchers [13,20,34]. The explanation points out that even one adsorbed atom causes a long-range oscillation in charge density at the Fermi level by breaking the local symmetry of wave functions, which in turn causes a wavy image like this one. This superstructure in the image is a consequence of the modified electronic structure of graphite around the hillock, which was detected by the STM. It does not imply a corresponding waviness in the atomic structure.

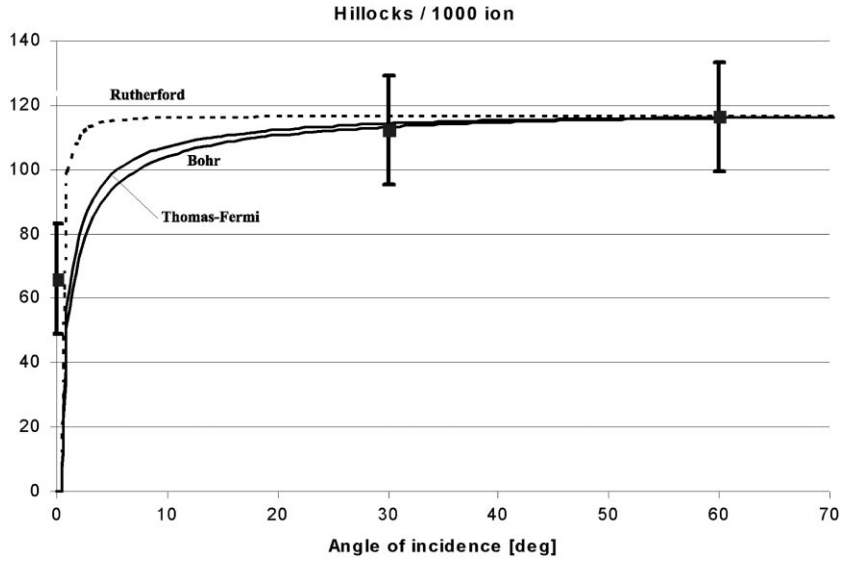

Fig. 6. Measured data of surface density of hillocks compared to scaled model calculations based on different scattering potentials (heavy squares indicate the experimental data) (see the appendix for details).

To get an acceptable statistics on hillock density on the sample surface, we investigated the surface carefully and found some other features, which are attributed to the irradiation. The elongated tracks in Fig. 5. are such features. They have the same height and width as hillocks (1–2 and 20–50 Å, respectively), and a length of about 500–1500 Å. These data point to the common origin of hillocks and tracks, which can be caused by a secondary or a higher-order knocked-on C atom channelling between the layers of the graphite [31].

4. Conclusion

We investigated the effect of irradiation with 246 MeV Kr^+ ions on HOPG at perpendicular, 30° and 60° inclined incidence. In all three cases hillocks were produced on the surface of the sample. At perpendicular incidence the density of hillocks was about 50% of that of the other samples. We attribute the hillock formation to the escape of primary or higher-order knocked-on C atoms leaving the sample. The difference observed in the surface density of hillocks is attributed to differences in the probability of scattering atoms towards the surface in the case of perpendicular incidence, as compared to other angles greater than 10–20°. On all of the investigated samples the density of hillocks is significantly lower than the ion dose, so it is unlikely that the hillocks are caused by incoming ions. We found elongated features, with height and width dimensions very close to those of hillocks. These features are attributed to secondary or higher-order knocked-on C atoms channelling between the upper layers of graphite.

Acknowledgements

This work was supported by OTKA grant No. T025928. The irradiation of the samples at the JINR-Dubna facility was supported by the Hungarian Academy of Sciences.

Appendix

A.1. Calculation of scattering cross-section

First we consider the rules of elastic scattering only. According to the representation used in [32] the scattering process is visualized in Fig. 7. The

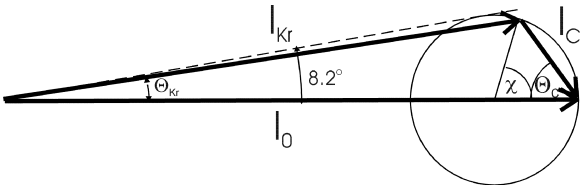

Fig. 7. Momentum diagram of the primary scattering process in the laboratory frame of reference. $\boldsymbol{I}_0$ is the momentum vector of primary Kr^+ ion, $\boldsymbol{I}_{Kr}$ and $\boldsymbol{I}_C$ are the momenta of scattered Kr^+ and C particles, respectively. Θ_{Kr} and Θ_C are the scattering angles in laboratory frame and χ the scattering angle in the centre-of-mass frame (see the appendix for more details).

primary Kr^+ ion with momentum $\boldsymbol{I}_0$ and energy E_0 collides with a C atom in the HOPG structure. The energy the C particle gets, is E_C and the corresponding momentum will be $\boldsymbol{I}_C$. The angle in laboratory frame of reference between $\boldsymbol{I}_C$ and $\boldsymbol{I}_0$ is χ. The energy of the incident Kr ion changes to E_{Kr} and its momentum will be $\boldsymbol{I}_{Kr}$, having a Θ_{Kr} angle with $\boldsymbol{I}_0$ in laboratory frame of reference. The conservation laws of energy and momentum are fulfilled if the sum of $\boldsymbol{I}_{Kr}$ and $\boldsymbol{I}_C$ vectors is equal to $\boldsymbol{I}_0$, and the intersection of the two vectors is on the circle drawn in Fig. 7, the radius of which is $r = I_0 m_C/(m_{Kr} + m_C)$ [32]. The angle χ is the scattering angle of the two particles in the centre-of-mass frame, and it determines both scattering angles in laboratory frame by the formulas

$$\Theta_{Kr} = \arctan\left(\frac{m_C \sin\chi}{m_{Kr} + m_C \cos\chi}\right), \quad \Theta_C = \frac{\pi - \chi}{2}.$$

The scattering angle Θ_{Kr} of the Kr ion is limited to 8.2° (angle between $\boldsymbol{I}_0$ and the tangent to the circle), the energy of the knocked-on (secondary) C particle is limited to 91.7 MeV at 0° scattering angle ($E_C = 4m_{Kr}m_C/(m_{Kr} + m_C)^2 E_0$). The energy E_C of the C particle is decreased by increasing the scattering angle Θ_C and it vanishes at $\Theta_C = 90°$. In perpendicular irradiation geometry the scattering angle needed for the escape of the C particle is larger than 90°; this means that in sample S1 no primary knocked-on C atom could leave the HOPG without further collision and consequently, the hillock formation should be caused by multiple scattering.

In the second step we consider the scattering process as Rutherford scattering (i.e. unscreened Coulomb scattering potential). The differential scattering cross-section in this case is given by the formula (Eq. (19.2) in [32])

$$d\sigma = \pi\left(\frac{\alpha}{E_0}\right)\frac{\cos\chi/2}{\sin^3\chi/2}\, d\chi,$$

where $\alpha = Z_{Kr}Z_C e^2$, Z_{Kr} and Z_C are the atomic numbers of the ions and e the electron charge. This formula is singular at $\chi = 0$, $\Theta_C = 90°$. The problem could be overcome taking into account the fact that the knocked-on C atom needs some energy to reach the surface and cause a hillock. We choose the arbitrary value of $E_C^{limit} = 10$ keV. In Fig. 7 the momentum is $I_C = 2r\sin(\chi/2)$; using the formula $E = I^2/2m$ for both E_C^{limit} and E_0 we get the formula

$$\sin^2\left(\frac{\chi}{2}\right) = \frac{E_C^{limit}(m_C + m_{Kr})^2}{E_0 \quad 4m_{Kr}m_C}.$$

Inserting the numerical values given above into this equation we get the limiting angles for the scattering as $\chi/2 > 0.54°$, or $\Theta_C < 89.46°$.

For simplicity, we assume that the probability of hillock formation is proportional to the cumulative scattering cross-section into the incidence-dependent angular range, which can reach the sample surface: $\sigma = \sigma(\Theta_C^{min}; \beta)$. The incidence angle β limits the scattering angle of the C particles at which the knocked-on C atom may cross the irradiated surface to $\Theta_C > 90° - \beta$ or $\chi/2 < \beta$. The integral

$$\sigma(\beta) = \text{Const.} \int_{min}^{\beta} \frac{\cos\chi/2}{\sin^3\chi/2}\, d\chi$$

is an elementary integral, but we integrated it numerically because of its compatibility with the formula obtained for the other scattering potentials.

We performed calculations based on more realistic screened scattering potentials too. We took the general formula of Nastasi et al. [2] for the differential scattering cross-section of a series of screened scattering potentials (Eqs. (4.61)–(4.65) in [2])

$$d\sigma = \text{Const.} \cdot \frac{f(\sin\chi/2)}{\sin^3\chi/2}\, d\left(\sin\frac{\chi}{2}\right).$$

The $f(\sin(\chi/2))$ function is a complicated function, but with our data it can be approximated by the formula

$$f\left(\sin\frac{\chi}{2}\right) = \text{Const.}\,\sin^{3/2-2m}\frac{\chi}{2}.$$

The exponent m is a function of the screening type, its extreme values are $m=1/3$ for the Thomas-Fermi approximation and $m=0.103$ for the Bohr approximation. Using the same limits for the Rutherford approximation, we integrated numerically the three functions for the approximations

$$\sigma(\beta) = \text{Const.}\int_{\Theta_{\min}}^{\beta}\frac{\cos\chi/2}{\sin^{3/2+2m}\chi/2}\,\mathrm{d}\chi.$$

The curves of $\sigma(\beta)$ versus β plotted in Fig. 6 are scaled in such a way that in the plateau region they have the same value as the experimental data corresponding to sample S3 (60° incidence). The solid lines in Fig. 6 correspond to the screened approximations, and the dotted ones to the Rutherford approximation. The curve is in good agreement with our measurements at 30° incidence. The difference at 0° incidence is accounted for by the fact that – as mentioned earlier – by this incidence no C particle can escape from the sample in a single scattering event.

References

[1] F.F. Komarov, Ion Beam Modification of Metals, Gordon and Breach Science Publishers, Philadelphia, 1992.
[2] M. Nastasi, J.W. Mayer, J.K. Hirvonen, Ion–Solid Interactions, University Press, Cambridge, 1996.
[3] S. Miyake, S. Watanabe, H. Miyazawa, M. Murakawa, R. Kaneko, T. Miyamoto, Appl. Phys. Lett. 65 (1994) 3206.
[4] A. Barna, Surf. Coat. Tech. 80 (1996) 89.
[5] K. Dehghan, Z. Shi, T.H. Woodrum, S. Brewer, R. Sacks, Appl. Spectrosc. 48 (1994) 553.
[6] S.C. Tjong, S.M. Zhu, Scr. Metall. Mater. 32 (1995) 535.
[7] G.R. Rao, E.H. Lee, B.A. Chin, L.K. Mansur, Metall. Mater. Trans. A 25 (1994) 193.
[8] G. Binnig, G. Rohrer, C. Gerber, E. Weibel, Phys. Rev. Lett. 49 (1982) 57.
[9] G. Binnig, Phys. Scr. 19 (1987) 53.
[10] R. Coratger, A. Claverie, A. Chahboun, V. Landry, F. Ajustron, J. Beauvillain, Surf. Sci. 262 (1992) 208.
[11] L. Porte, M. Phaner, C.H. deVilleneuve, N. Moncoffre, J. Tousset, Nucl. Instr. and Meth. 44 (1989) 116.
[12] L. Porte, C.H. deVilleneuve, M. Phaner, J. Vac. Sci. Technol. B 9 (1991) 1064.
[13] S. Bouffard, J. Cousty, Y. Pennec, F. Thibaudau, Radiat. Effects Defects Solids 126 (1993) 225.
[14] L.P. Biró, J. Gyulai, K. Havancsák, Phys. Rev. B 52 (1995) 2047.
[15] L.P. Biró, J. Gyulai, K. Havancsák, Nucl. Instr. and Meth. B 112 (1996) 270.
[16] L.P. Biró, J. Gyulai, K. Havancsák, A.Y. Didyk, S. Bogen, L. Frey, Phys. Rev. B 54 (1996) 11853.
[17] T. Li, B.V. King, R.J. MacDonald, G.F. Cotterill, B.J. O'Connor, R. Lang, Surf. Sci. 312 (1994) 399.
[18] R. Coratger, A. Claverie, F. Ajustron, J. Beauvillain, Surf. Sci. 227 (1990) 714.
[19] I.H. Wilson, N.J. Zheng, U. Knipping, I.S.T. Tsong, Phys. Rev. B 38 (1988) 8444.
[20] J.J. Yan, Z.G. Li, C.Y. Bai, W.S. Yang, Y.G. Wang, W.J. Zhao, Y.X. Kang, F.C. Yu, P.J. Zhai, X.W.J. Tang, Appl. Phys. 75 (1994) 1390.
[21] L.T. Chadderton, H. Montagu-Pollock, Proc. Roy. Soc. London Ser. A 274 (1969) 239.
[22] R.L. Fleischer, P.B. Price, R.M.J. Walker, Appl. Phys. 36 (1965) 3645.
[23] H. Ogiso, H. Tokumoto, S. Nakano, K.J. Yamanaka, Vac. Sci. Technol. B 16 (1998) 1914.
[24] J. Krim, I. Heyvaert, C. van Heasendock, Y. Bruynseraede, Phys. Rev. Lett. 70 (1993) 57.
[25] D. Takeuchi, T. Seki, T. Aoki, J. Matsuo, I. Yamada, Mater. Chem. Phys. 54 (1998) 76.
[26] L.P. Biró, J. Gyulai, K. Havancsak, A.Y. Didyk, S. Bogen, L. Frey, H. Ryssel, Nucl. Instr. and Meth. 122 (1997) 559.
[27] L.P. Biró, J. Gyulai, K. Havancsák, Vacuum 50 (1998) 263.
[28] L.P. Biró, J. Gyulai, K. Havancsák, Nucl. Instr. and Meth. 122 (1998) 476.
[29] S.G. Hall, M.B. Nielsen, R.E. Palmer, J. Appl. Phys. 83 (1998) 733.
[30] T. Seki, T. Kaneko, D. Takeuchi, T. Aoki, J. Matsuo, Z. Insepov, I. Yamada, Nucl. Instr. and Meth. 121 (1997) 498.
[31] K. Havancsák, L.P. Biró, J. Gyulai, Z. Illes, J. Nucl. Mater. 251 (1998) 139.
[32] L.D. Landau, E.M. Lifschitz, Lehrbuch der theoretischen Physik I: Mechanik, Akademie Verlag, Berlin, 1973.
[33] H.A. Mizes, J.S. Foster, Science 244 (1989) 559.
[34] J. Xhie, K. Sattler, U. Müller, N. Venkateswaren, G. Raina, Phys. Rev. B 43 (1991) 8917.